Journal of Power Sources 243 (2013) 1–9

Contents lists available at SciVerse ScienceDirect

Journal of Power Sources

journal homepage: www.elsevier.com/locate/jpowsour

Operational characteristics of thin film solid oxide fuel cells with ruthenium anode in natural gas

Yuto Takagi [a,b,*], Kian Kerman [a], Changhyun Ko [a], Shriram Ramanathan [a]

[a] Harvard School of Engineering and Applied Sciences, Harvard University, Cambridge, MA 02138, USA
[b] Advanced Material Laboratories, Sony Corporation, Atsugi, Kanagawa 243-0021, Japan

HIGHLIGHTS

- Thin film micro-SOFCs with Ru anodes were fabricated and operated with dry natural gas and methane.
- Peak power density of 800 mW cm^{-2} at 530 °C was obtained with weakly humidified natural gas.
- Quasi-periodic oscillatory behavior was observed under methane operation.
- Difference in Ru surface oxidation states was found by post-operation XPS.

ARTICLE INFO

Article history:
Received 25 March 2013
Received in revised form
28 May 2013
Accepted 1 June 2013
Available online 10 June 2013

Keywords:
Ruthenium
Solid oxide fuel cells
Thin films
Natural gas
Methane
XPS

ABSTRACT

Direct utilization of hydrocarbons in low temperature solid oxide fuel cells is of growing interest in the landscape of alternative energy technologies. Here, we report on performance of self-supported micro-solid oxide fuel cells (μSOFCs) with ruthenium (Ru) nano-porous thin film anodes operating in natural gas and methane. The μSOFCs consist of 8 mol% yttria-stabilized zirconia thin film electrolytes, porous platinum cathodes and porous Ru anodes, and were tested with dry natural gas and methane as fuels and air as the oxidant. At 500 °C, comparable power densities of 410 mW cm^{-2} and 440 mW cm^{-2} were obtained with dry natural gas and methane, respectively. In weakly humidified natural gas, open circuit voltage of 0.95 V at 530 °C with peak power density of 800 mW cm^{-2} was realized. The μSOFC was continuously operated at constant voltage of 0.7 V with methane, where quasi-periodic oscillatory behavior of the performance was observed. Through post-operation XPS studies it was found that the oxidation state of Ru anode surfaces significantly differs depending on the fuel used, oxidation being enhanced with methane or natural gas. The nature of the oscillation is discussed based on the transition in surface oxygen coverage states and electro-catalytic activity of Ru anodes.

1. Introduction

Direct oxidation of hydrocarbon fuels in solid oxide fuel cells (SOFCs) is an active area of research as it would allow removal of fuel reformers and simplify overall system integration [1–5]. Methane-fueled SOFCs with weak or no humidification have received considerable attention in the scientific community due to the abundance and accessibility of the fuel [6–10]. For recent examples, Chen et al. [6] showed an open circuit voltage (OCV) of 0.6 V and power density of 60 mW cm^{-2} at 750 °C with a perovskite $La_{0.75}Sr_{0.25}Cr_{0.5}Mn_{0.5}O_3$–Gd-doped Ceria (LSCM–CGO) anode using 3% humidified methane as fuel, while Wang et al. [9] reported an OCV of 0.8 V and power density of 460 mW cm^{-2} at 650 °C with Ru–$Ce_{0.8}Sm_{0.2}O_{1.9}$ (SDC) catalytic layer also supplying 3% humidified methane. It has been pointed out that operation with dry hydrocarbons above 700 °C potentially results in problematic carbon coking [8]. Therefore, it is of importance to improve the fuel cell performance in the ~600 °C temperature range. However, decreasing the temperature may result in an increase of area-specific resistivity (ASR), which could in turn decrease the cell performance. Besides the contribution of kinetic losses from the electrodes, there is also Ohmic loss related to oxygen ion transport through the electrolyte [11]. Lowering operation temperature of SOFCs can be achieved by reducing the electrolyte thickness and using improved electrode materials. Micro-SOFCs (μSOFCs) with sub-micrometer thick electrolytes have demonstrated improved

* Corresponding author. Advanced Material Laboratories, Sony Corporation, Atsugi, Kanagawa 243-0021, Japan. Tel.: +81 50 3141 1797; fax: +81 50 3809 2000.
E-mail addresses: ytakagi@seas.harvard.edu, yuto.takagi@jp.sony.com (Y. Takagi), shriram@seas.harvard.edu (S. Ramanathan).

0378-7753/$ – see front matter © 2013 Elsevier B.V. All rights reserved.
http://dx.doi.org/10.1016/j.jpowsour.2013.06.002

performance in the 400–600 °C temperature range [12–14]. Such small scale fuel cells also have relevance to applications in mobile energy and are an emerging field of active research.

Ruthenium (Ru) is known to be an excellent catalyst for steam and dry reforming [15,16], partial oxidation of methane [17–20], and has been utilized for direct hydrocarbon oxidation in SOFCs [10,21–23]. Fig. 1 schematically provides possible reactions paths for methane oxidation over Ru based anodes in SOFCs that have been discussed in literature [10,15,16,24–26]. As pointed out by Marina and Mogensen [27] and Park et al. [28], electrochemical oxidation of methane is unlikely to occur in a single step. The first possible route of methane oxidation is a process that involves C–H bond cracking followed by electrochemical oxidation of the products (shown in Fig. 1(a)). However, Ru is known to be rather inactive to hydrocarbon cracking [29]. Another probable route of methane oxidation on Ru electrodes is partial oxidation combined with reforming and electrochemical oxidation of intermediates (shown in Fig. 1(b)). Partial oxidation and steam or dry reforming of methane produces intermediate reactants such as hydrogen (H_2) and carbon monoxide (CO). These can be oxidized to generate water (H_2O) and carbon dioxide (CO_2) which further aids methane reforming. Within this scheme, the overall reaction cycles are locally coupled and accelerated [24]. Ru is active to these reactions and resistant to carbon deposition [16], and appears to be a promising anode material for direct hydrocarbon utilization in SOFCs. In previous studies, fabrication and performance of porous Ru anodes [23] and Ru–CGO composite anodes [22] on μSOFC platforms were investigated with humidified methane as the fuel. In this study, μSOFCs incorporating porous Ru metal anode operated with dry natural gas and methane are demonstrated and directly compared. At 500 °C, comparable power densities are obtained with methane and natural gas. In weakly humidified natural gas, a peak power density of 800 mW cm^{-2} was obtained. Extended constant voltage operation was investigated with methane fuel, where intermittent cell current oscillation was observed. The instability is discussed with regard to the oxidation state of the Ru anode catalysts, based on post-operation X-ray photoelectron spectroscopy (XPS) analysis.

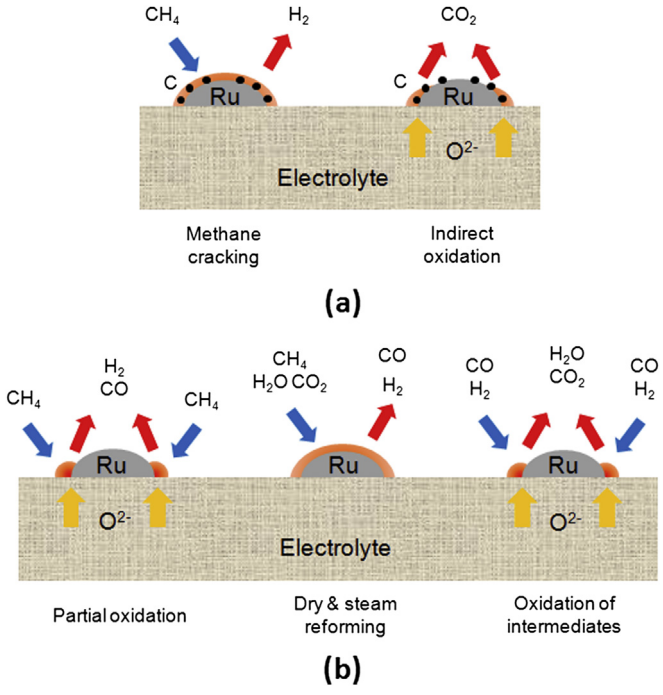

Fig. 1. Possible reactions paths of methane and its intermediate species over Ru electrodes, (a) cracking followed by in-direct oxidation, and (b) partial oxidation, reforming and oxidation of intermediate species. Ru can catalyze various hydrocarbon involved reactions as noted in literature [15–20].

2. Experimental details

2.1. Fabrication of Ru anode thin film μSOFCs

$10 \times 10 \times 0.5$ mm^3 silicon nitride-coated silicon (Si_3N_4-coated Si) substrates were used as a platform for μSOFC fabrication. Each substrate was processed to have nine 200 μm × 200 μm free-standing Si_3N_4 membranes. As shown in Fig. 2, thin film μSOFC fabrication process starts with depositing thin film 8 mol% yttria-stabilized zirconia (YSZ) electrolytes on Si_3N_4. YSZ was deposited in argon (Ar) at a pressure of 5 mTorr and power of 100 W by radio frequency magnetron sputtering for 65 min. The target consisted of a circular pellet, two inches in diameter, with composition of Y_2O_3 8 mol%:ZrO_2 92%. The substrate was heated to a temperature of 550 °C. Porous thin film platinum (Pt) cathodes were deposited on top of YSZ electrolytes in Ar at a pressure of 75 mTorr and power of 250 W by direct current (DC) magnetron sputtering for

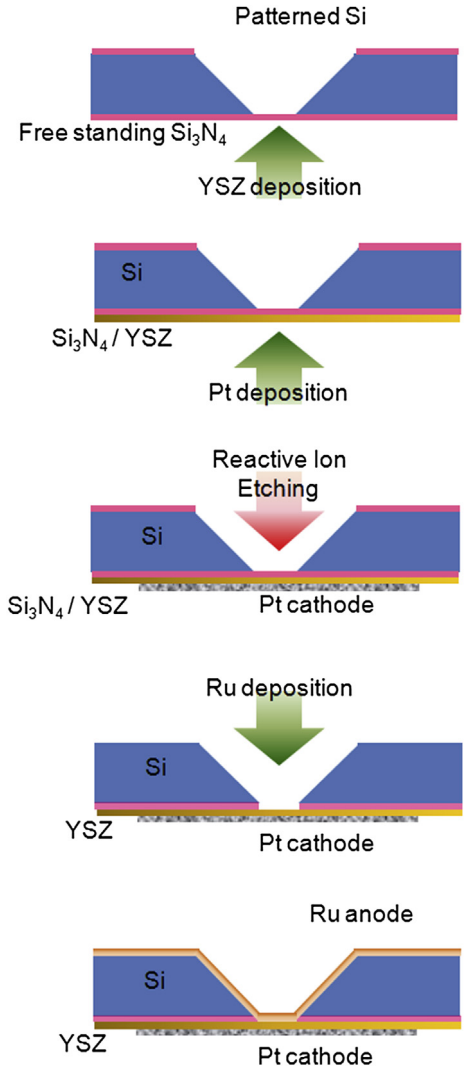

Fig. 2. Fabrication process flow of Ru anode–YSZ electrolyte–Pt cathode thin film μSOFC on a silicon platform.

10 min without substrate heating. After removal of the Si_3N_4 layer by reactive ion etching in oxygen (O_2) and tetrafluoromethane environment, porous thin film Ru anodes were deposited on self-supported YSZ–Pt bilayers in Ar at a pressure of 75 mTorr and power of 250 W by DC magnetron sputtering for 18.5 min without substrate heating. Deposition rates of YSZ, Pt and Ru thin films were calibrated by X-ray reflectivity (XRR) with a Bruker D8 X-ray Diffractometer in parallel beam geometry.

2.2. Performance measurements and post-operation analyses on thin film μSOFCs

μSOFCs were tested in a fuel cell test station, configured as depicted in Fig. 3. The anode side of the μSOFC was sealed by a gold ring, whereas the cathode side was exposed to air. The fuel supply lines were designed to be able to switch between three fuels: natural gas, methane, and hydrogen. A humidifier filled with de-ionized water and a bypass line allowed direct or 3% humidified fuel supply. Dry 5% H_2/Ar gas was supplied to the anodes of the μSOFCs at a flow rate of 50 ml min^{-1} during temperature ramp. When a temperature of 300 °C was reached, dry methane was fed at a flow rate of 50 ml min^{-1} for fuel cell tests with methane and natural gas. When a temperature of 450 °C was reached, methane was further switched to dry natural gas fed at a flow rate of 50 ml min^{-1} for fuel cell tests with natural gas. These gas switching procedures were used to confirm OCV at low temperature, and to avoid accelerated morphology change of the porous metal thin film during temperature ramp under a hydrogen atmosphere [23]. The sulfur content in pipeline supplied natural gas was ~0.0017% by weight. Current collection from individual μSOFC cells was done by contact probes. No additional current collector was applied, utilizing in-plane conduction through deposited electrodes (Pt for cathode, Ru for anode). Current–voltage (*I–V*) measurements were carried out during the temperature ramp. Extended operation for 300 min was performed at a constant voltage of 0.7 V between the anode and the cathode with a Solartron 1287A operated in potentiostatic mode, while keeping the μSOFC temperature constant.

The morphology of Ru anodes was investigated with Carl Zeiss Ultraplus Field Emission Scanning Electron Microscopy (SEM) after the fuel cell measurements. The oxidation states of Ru anodes were investigated with XPS using a SSX-100 ESCA XPS system equipped with a monochromated Al Kα X-ray source (1.4866 keV) in high vacuum (~10^{-8} Torr). XP spectra of the Ru 3d, Ru 3p and Oxygen (O) 1s emissions were obtained with the pass energy at 100 eV and an X-ray spot size of 150 μm. The Ru films were grounded to the sample holder to avoid charging effects. The data was fitted with CasaXPS program package using mixed Gaussian–Lorentzian peak shapes and a Shirley background. The signal intensity of O 1s and Ru 3d spectra was normalized against corresponding Ru 3p peak area. The O 1s emission was deconvoluted into contributions from different species, while full width at half maximum (FWHM) was limited in a narrow range. Trends in the atomic concentrations of different oxygen species were estimated by comparing the corresponding O 1s peak areas against the Ru 3p peak area using tabulated sensitivity factors, 2.93 for O 1s and 10.2 for Ru 3p.

3. Results and discussion

3.1. Performance of porous Ru anode μSOFCs in methane and natural gas

A representative optical image of μSOFCs fabricated for this work is shown in Fig. 4(a). The typical effective working area of a μSOFC cell was 200 μm × 200 μm as measured by SEM. The symmetrical buckling pattern results from residual compressive film stress due to YSZ deposition conditions. These buckling patterns are typically observed in thermo-mechanically stable self-supported thin film μSOFCs [22,23,30,31].

Prior to evaluating the fuel cell performance under different fuels, electrode and electrolyte thicknesses were optimized to maximize the OCV and power density with methane fuel. Porous metal electrodes require sufficient in-plane conductivity and high triple phase boundary density (interface at YSZ electrolyte, metal electrode and gas) [23]. These factors are controlled by the porosity and thickness of the electrode. The electrolyte thickness must also be optimized as thicker electrolytes may prevent electronic and gas leakage, but concurrently lead to higher Ohmic loss [12]. The Ru anode thickness was optimized to ~50 nm, YSZ electrolyte to ~110 nm and Pt cathode to ~70 nm. A typical cross sectional view of a μSOFC after fuel cell operation is shown in Fig. 4(b). Good adhesion between electrolyte and electrodes is observed without detachment or cracks between the layers.

Fig. 5(a) and (b) shows OCV, peak power density and *I–V* characteristics of the μSOFC operated in dry methane fuel, measured from 410 °C to 525 °C. The fuel cell had a maximum power density of 635 mW cm^{-2} with OCV of 0.91 V at 525 °C, respectively. The OCV value increases with temperature up to 500 °C, which may be due to the gradual formation of in-plane current collection paths within the porous electrodes during the temperature ramp as observed in prior work [23]. Once an interconnect porous network is formed, the OCV is stable [12]. Performance of the fuel cell operated with dry natural gas is shown in Fig. 6(a) and (b), in the 410–500 °C temperature range. The fuel cell exhibited a maximum power density of 410 mW cm^{-2} with OCV of 0.96 V at 500 °C. The OCV slightly decreased by 30 mV when fuel was switched from

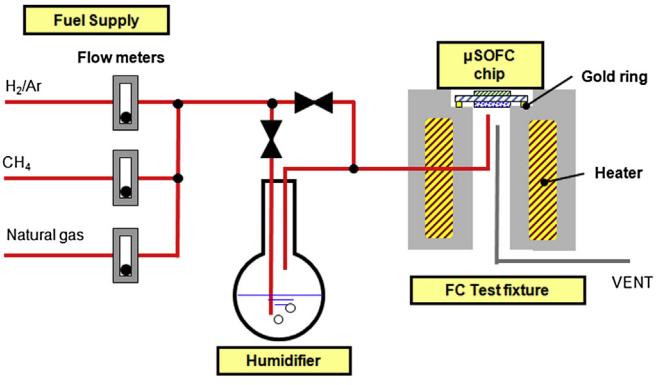

Fig. 3. Schematic diagram of the fuel cell test station, fuels can be switched and humidifier can be connected/disconnected during the testing.

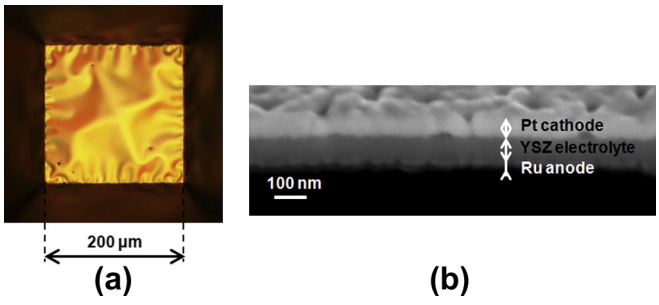

Fig. 4. (a) Optical micrograph of self-supported μSOFC with porous Ru thin film anode, taken from the anode side. Buckling is due to the residual compressive stress typical in such membranes. (b) Focused ion beam (FIB) cross-section SEM micrograph of a μSOFC.

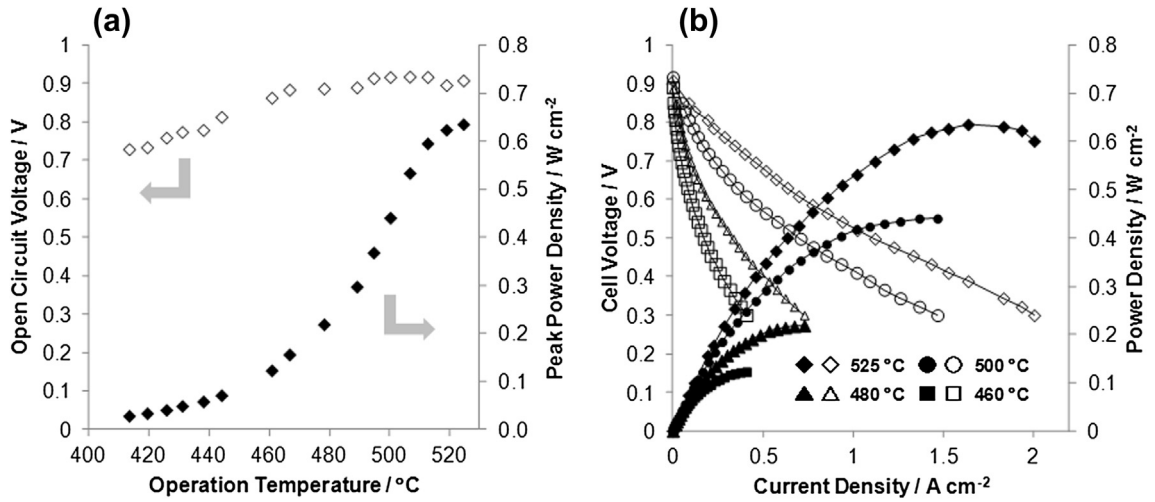

Fig. 5. (a) OCV, peak power density, and (b) *I–V* characteristics of the Ru anode μSOFC operated with dry methane, measured between cell temperatures of 410 °C and 525 °C. Highest power density achieved was 635 mW cm^{-2} with OCV of 0.91 V at 525 °C.

methane to natural gas, possibly due to impurities present in natural gas. Performance at 530 °C with 3% humidified natural gas is depicted in Fig. 6(c). Under this condition, the highest power density achieved was 800 mW cm^{-2} at OCV of 0.95 V. As a comparison, Wang et al. [9] reported power density of 330 mW cm^{-2} at 600 °C with humidified methane and Ru–SDC/nickel (Ni)–SDC anode. Liu and Barnett [8] demonstrated power density of 90 mW cm^{-2} at 600 °C with humidified natural gas and

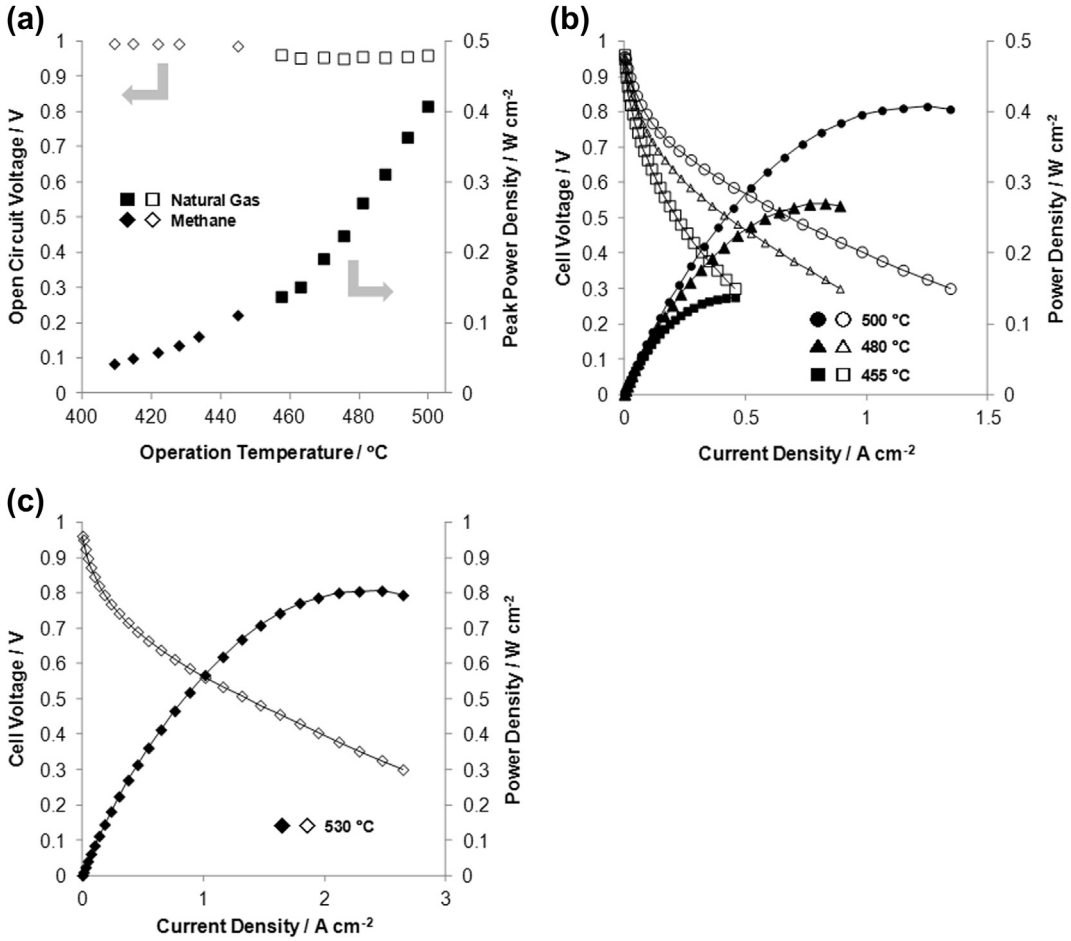

Fig. 6. (a) OCV, peak power density, and (b) *I–V* characteristics of the Ru anode μSOFC operated with dry natural gas, measured between cell temperatures of 410 °C and 500 °C, and (c) *I–V* characteristics of the Ru anode μSOFC operated with 3% humidified natural gas, measured at cell temperature of 530 °C. Highest power density achieved was 410 mW cm^{-2} with OCV of 0.96 V at 500 °C with dry natural gas, and 800 mW cm^{-2} with OCV of 0.95 V with humidified natural gas.

Ni–YSZ anode. The improvement in the maximum power density by a factor larger than two at lower operation temperatures may be attributed to the use of sub-micrometer scale electrolytes and the high electro-catalytic activity of nano-porous Ru anode toward methane oxidation.

OCV and peak power densities with dry natural gas and dry methane at different temperatures are summarized in Table 1. Peak power densities with natural gas and methane were comparable, suggesting minor effect from the additional species present in natural gas on the Ru anodes within the period of the measurement. The power densities were comparable to previous results with humidified methane [23]. The theoretical OCV calculated from the Nernst equation for complete oxidation of methane is 1.13 V, assuming partial pressures of methane equal to 0.97 atm, H_2O as 0.03 atm, and CO_2 as 0.001 atm. In the case of partial oxidation of methane to CO and H_2O, the theoretical OCV is 1.05 V assuming the same partial pressures for methane and water and 0.001 atm for CO. The OCVs obtained in this work indicate that the partial oxidation is more likely, which agrees well with previous reports [27,28,32]. The remaining difference of OCVs at 495 °C compared to the theoretical value could be explained by possible existence of minute electronic leakage through nano-metric YSZ electrolytes, or by the possibility that methane oxidation is not reaching equilibrium in the low temperature regime [6]. However, the OCVs obtained in this work are similar to those obtained with electrolytes having a thickness two orders of magnitude larger and operated at higher temperature [8–10].

Fig. 7 depicts morphology of nano-porous Ru anodes after the fuel cell tests with (a) methane and (b) natural gas fuels. Both anodes showed typical two-dimensional nano-porous morphology with no clear difference. No observable carbon deposition, such as carbon fibers [33], was detected. Ru based catalysts are indeed known to be resistant to carbon deposition from methane [17,22,23]. Furthermore, low operation temperature (<650 °C) helps to suppress carbon deposition [8].

3.2. Oscillatory characteristics of methane fueled μSOFC

μSOFCs were operated at a constant applied voltage of 0.7 V at 455 °C. Fig. 8(a) presents fuel cell current evolution during extended operation with 3% humidified methane as fuel. Quasi-periodic oscillations in the fuel cell current were observed. These oscillations did not occur during operation with hydrogen fuel. The periods of the oscillations ranged between 10 and 50 min. One period consisted of a slow current decay followed by a sudden recovery. Oscillatory catalytic behaviors in methane oxidation have been observed with RuO_x–YSZ catalysts [17], palladium–alumina (Pd–Al_2O_3) catalysts [34], and with Pt doped mixed oxide catalysts [20]. The mechanism of oscillatory behavior is not fully understood, however published work indicates that methane activation and in turn the electrochemical performance is highly dependent on the oxidation state of the catalyst surface. For Ru based catalysts, it is known that reduced metallic sites mainly contribute in methane conversion by partial oxidation while oxidized Ru sites facilitate complete oxidation with lower activity [18]. Bebelis et al. [17] found that the oscillatory behavior observed in methane oxidation over a RuO_x–YSZ electrode is related to transitions between different oxidation states of Ru. The surface oxidation state of the electrode was correlated to the anode potential, a more negative potential indicating a lower surface oxygen activity and a higher degree of reduction. The Ru catalyst showed improved electro-catalytic rate and higher selectivity to partial oxidation with a greater degree of reduction.

Table 1
Open circuit voltage (OCV) and peak power density of Ru anode μSOFCs at different cell temperatures operated with dry natural gas and dry methane. OCV and power densities were comparable between natural gas and methane.

Cell temperature (°C)	Natural gas		Methane	
	OCV (V)	Peak power density (W cm^{-2})	OCV (V)	Peak power density (W cm^{-2})
465	0.95	0.16	0.88	0.14
475	0.95	0.22	0.89	0.20
485	0.95	0.30	0.89	0.27
495	0.96	0.37	0.91	0.37
500	0.96	0.41	0.92	0.44

In order to investigate the effect of the oxidation state of Ru, XPS was carried out on the Ru fuel cell anodes with different operation history. Fig. 9 shows Ru 3d core level spectra obtained from Ru anodes. They are characterized by a pair of relatively narrow peaks corresponding to the 5/2 and 3/2 spin–orbit components located at 279.0 and 283.2 eV, respectively. Operation in dry hydrogen has two effects on the appearance of the spectra (shown in Fig. 9(B)). The Ru 3d peaks appear sharper (decrease in FWHM), and the peaks show a shift to lower binding energy (B.E.). These are due to decreased signal from oxidized Ru species compared to the as-prepared sample (shown in Fig. 9(A)). On the contrary, after operation with methane (shown in Fig. 9(C)) the spectra appear wider with a shift to higher B.E., indicating further oxidation. Fig. 10 shows high resolution O 1s core spectra recorded from Ru anodes, (A) as prepared, (B) after operation with dry hydrogen at 455 °C, and (C) after operation with 3% humidified methane at 455 °C. The influence of the fuel on the oxidation state was investigated by deconvolution of O 1s spectra. Based on previous reports, the component at lower binding energy (529.1 +/− 0.3 eV) is attributed to O^{2-} species [35–37]. For metallic oxides such as RuO_2, final state effect gives rise to an asymmetry in the O 1s core level spectra [35,38–40]. The O^{2-} component was therefore fit with an asymmetric tail at high binding energies. Other components were fit with typical Gaussian–Lorentzian peak shapes. The higher binding energy component at 530.8 +/− 0.3 eV is attributed to OH^- species [38,41,42], which likely originates from water produced by fuel oxidation or present in the humidified fuel feed. The spectrum from a sample operated with methane (Fig. 10(C)) shows a third component at 532.2 eV. This component has been observed by O'Grady et al. [43], Sharma and Hines [44], and Shen et al. [45]. Kim et al. [35] attributed it to be due to the presence of absorbed water and/or oxygen containing compounds such as CO. Foelske et al. [41] attributed this peak to surface adsorbed H_2O. We extended our analysis by comparing the O 1s core spectra from Ru anodes operated with humidified fuels at higher temperature. Fig. 11 shows the spectra from Ru anodes, (A) as-prepared, (B) operated with 3% humidified hydrogen, (C) with 3% humidified methane, and (D) with 3% humidified natural gas, at 530 °C. The peak at 532.2 eV was not observed after operation with humidified hydrogen, but appears after operation with methane or natural gas. This suggests that the peak is not related to the presence of adsorbed water but rather, is due to oxygen containing compounds such as CO, or other intermediate products of the methane oxidation. The results of analyses on surface oxygen species after operation with different fuels are shown in Fig. 12. Oxygen species detected on the Ru anode surface after fuel cell operations are strongly affected by the fuel that is used to operate the cells, as summarized below:

1) Operation with dry hydrogen reduces the Ru electrode surface and the O^{2-} peak intensity (see Fig. 10(B)). Hydrogen is highly reactive with oxygen species and cleans the Ru surface by reacting with surface oxygen. When humidified hydrogen is

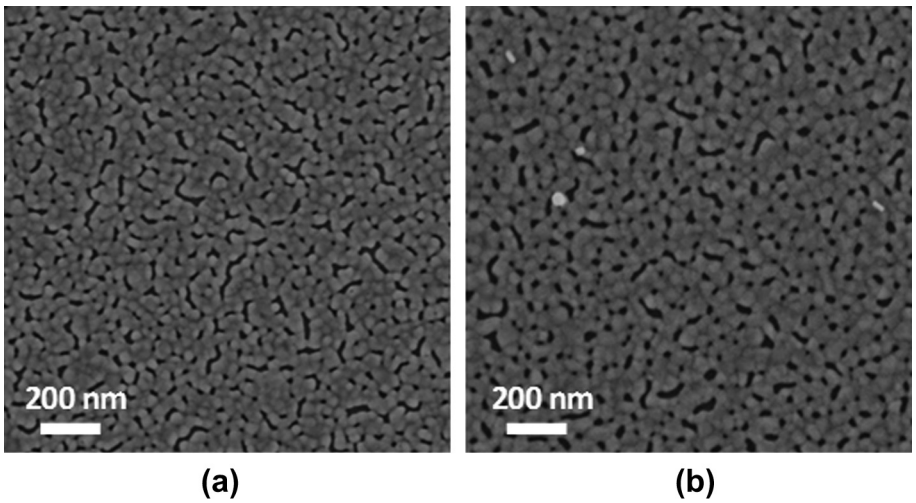

Fig. 7. SEM micrographs of Ru anodes on μSOFCs, (a) after operation with methane, and (b) after operation with natural gas, no obvious difference in morphology is observed.

supplied at 530 °C, a stronger OH^- peak is observed (see Fig. 11(B)). OH^- species may originate from H_2O added in the fuel stream and from fuel oxidation. No appearance of the higher binding energy peak (532.2 eV) was observed.

2) Operating with methane or natural gas significantly increases the O^{2-} component intensity (see Figs. 10(C), 11(C) and (D)). There appears to be greater amount of oxygen coverage on the Ru surface since oxygen adsorption is favored compared to methane under the experimental conditions. The peak at 532.2 eV appears and is related to CO or other oxygen related intermediates of the methane oxidation. No significant difference in photoelectron spectra was observed between anodes operated with methane (Fig. 11(C)) and natural gas (Fig. 11(D)). No sulfur related peak was detected.

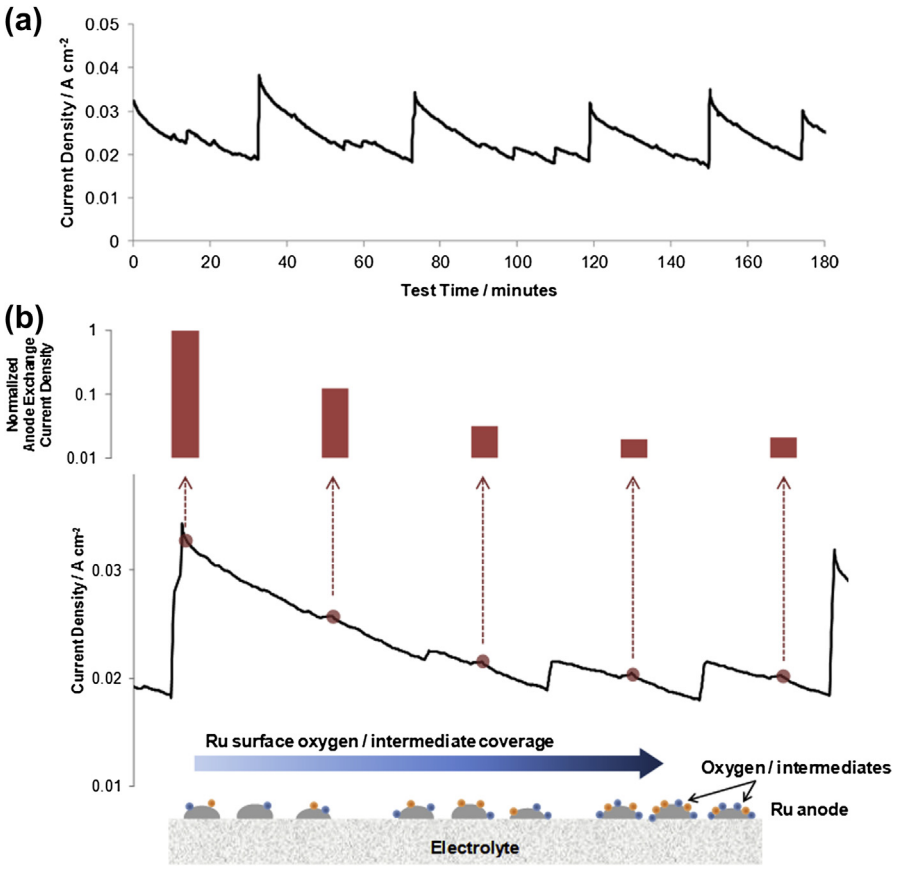

Fig. 8. (a) Fuel cell current history during extended operation with 3% humidified methane as fuel, at cell temperature of 455 °C and cell voltage of 0.7 V, quasi-periodic oscillations were observed. (b) Fuel cell current history during test time of 70–120 min, with normalized effective anode exchange current density and schematic of catalyst surface coverage states. Strong correlation of effective exchange current density and the fuel cell current density is observed.

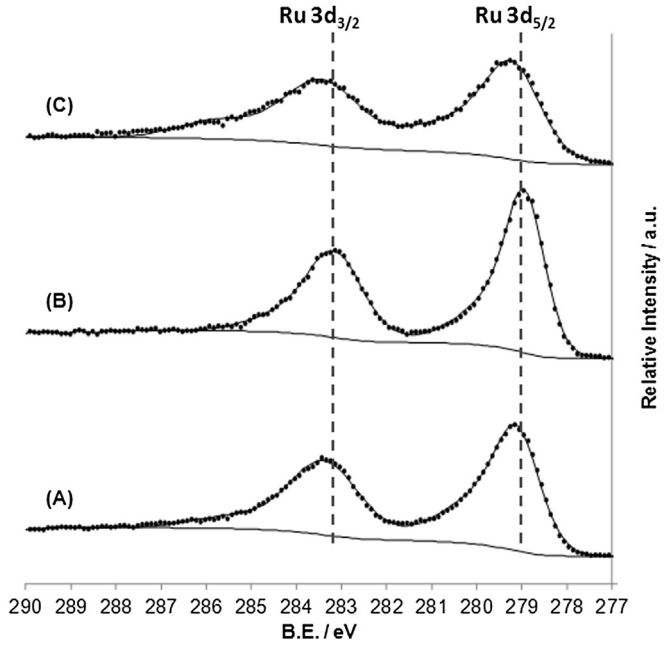

Fig. 9. High resolution Ru 3d spectra recorded from μSOFC Ru anodes by XPS, (A) as-prepared, (B) after operation in dry hydrogen at 455 °C, and (C) after operation in 3% humidified methane at 455 °C.

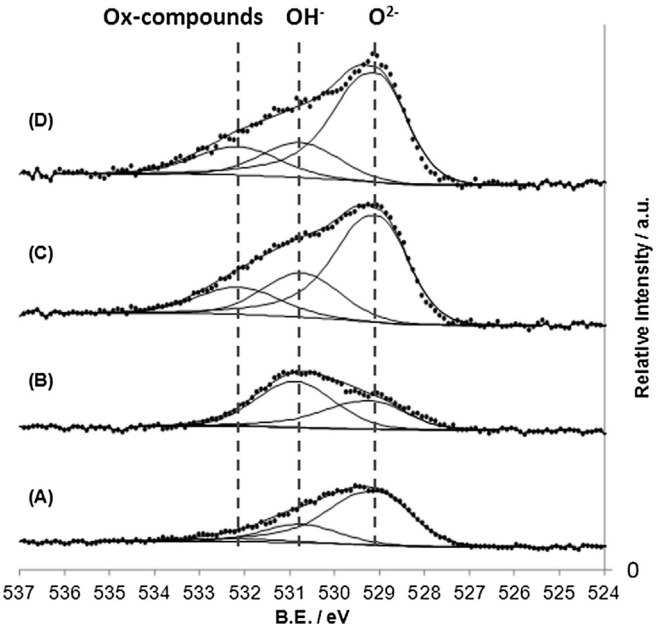

Fig. 11. High resolution O 1s spectra recorded from μSOFC Ru anodes by XPS, (A) as prepared, (B) after operation with 3% humidified hydrogen at 530 °C, (C) after operation with humidified methane at 530 °C, and (D) after operation with humidified natural gas at 530 °C. Increase of the O^{2-} peak intensity at 529.1 eV and appearance of the third peak at 532.2 eV is observed with both methane and natural gas fuels, whereas increase in OH^{-} peak at 530.8 eV was observed with humidified hydrogen.

3.3. Potential origin of the oscillatory behavior

Extensive oxygen coverage and appearance of the 3rd peak at higher B.E. on the Ru anode after methane and natural gas operation suggests that the oscillatory behavior observed may be due to the accumulation of an oxidized Ru layer and oxygen related intermediates on the metal surface. The current decay during one oscillation can be explained by a decrease of the anode exchange current density. In the following, only the effective exchange current density based on geometric electrode area is discussed. In the Tafel region, the anode overvoltage–current density relationship for the reduced surface can be described as,

$$\eta_{an} = a_{Red} \ln \frac{j^{Red}}{j_0^{Red}} \quad (1)$$

where η_{an} is the anode overvoltage, a_{Red} a constant, j_0^{Red} the exchange current density and j^{Red} the fuel cell current density. For a surface covered with an oxidized layer or oxygen related intermediates, the relationship changes to the following:

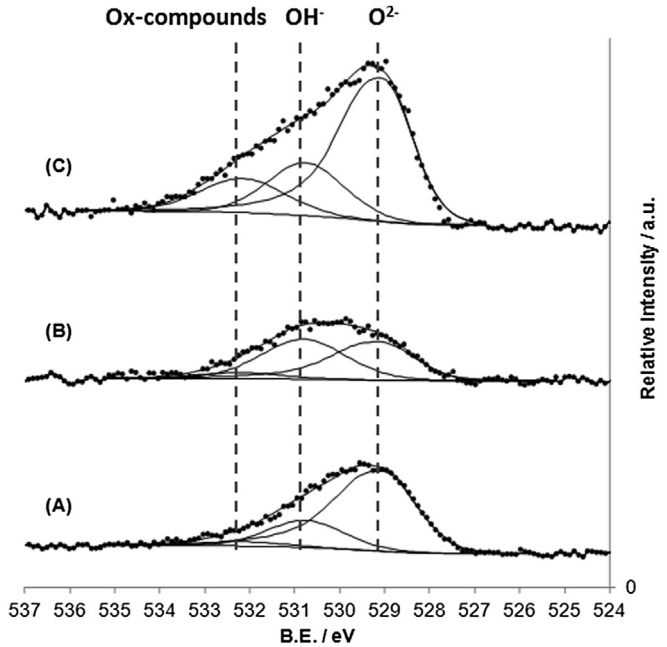

Fig. 10. High resolution O 1s spectra recorded from μSOFC Ru anodes by XPS, (A) as prepared, (B) after operated with dry hydrogen at 455 °C, and (C) after operated with 3% humidified methane at 455 °C. Intensity of O^{2-} peak centered at 529.1 eV increased after methane operation with appearance of the third peak at 532.2 eV.

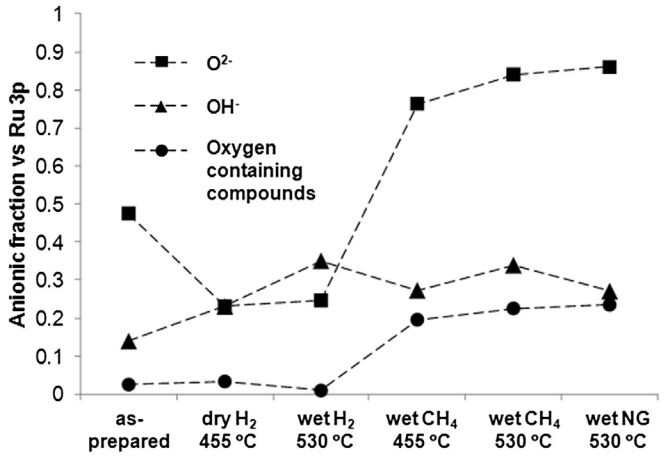

Fig. 12. Relative intensity of oxidic species peaks on Ru anode relative to Ru 3p peak as a function of μSOFC operation condition. Peak intensities of O^{2-} and oxygen containing compounds show increase after methane and natural gas operation, while O^{2-} peak decreases after hydrogen operation.

$$\eta_{an} = a_{Ox}\ln\frac{j^{Ox}}{j_0^{Ox}} \quad (2)$$

Here a_{Ox} is a constant, j_0^{Ox} the exchange current density, and j^{Ox} the current density at the surface covered with oxidized layer or oxygen related intermediates. As the portion x ($0 < x < 1$) of the Ru–YSZ interface becomes covered, the area averaged current density (j_{av}) will change to,

$$j_{av} = (1-x)j^{Red} + xj^{Ox} \quad (3)$$

$$j_{av} = (1-x)\exp\left(\frac{\eta_{an}}{a_{Red}}\right)j_0^{Red} + x\exp\left(\frac{\eta_{an}}{a_{Ox}}\right)j_0^{Ox} \quad (4)$$

Since the catalytic performance of reduced metallic sites is significantly better than the oxygen covered sites [17,18] we can expect $j_0^{Red} \gg j_0^{Ox}$. This indicates that increase in Ru surface oxygen coverage leads to an almost linear reduction in average current density under fixed anode overvoltage. The area averaged exchange current density $j_0^{av} = (1-x)j_0^{Red} + xj_0^{Ox}$ takes a value between j_0^{Ox} and j_0^{Red} depending on the surface coverage condition. In the Tafel region the fuel cell voltage E_{cell} at current j can be described as follows, where E_T^0 is the theoretical OCV at temperature T, η_{ca} the cathode over potential, and R_{ohm} the Ohmic resistance of the cell.

$$E_{cell} = E_T^0 - \eta_{an}(j) - \eta_{ca}(j) - jR_{ohm} \quad (5)$$

By comparing two I–V curves at a same current point obtained at different anode oxygen coverage states, we can expect cathode overvoltages and Ohmic losses to be constant assuming the cathode exchange current density remains constant [46]. According to (5) this implies that $\eta_{an}(j)$ must change accordingly. Normalized area averaged exchange current densities can be obtained by following relationship where a is treated as a constant, and superscripts 0 and 1 indicating different anode oxidation states.

$$\eta_{an}^0(j) - \eta_{an}^1(j) = a\ln\frac{j_0^1}{j_0^0} \quad (6)$$

The normalized exchange current densities derived from I–V measurements are shown with the schematics of Ru surface oxidation in Fig. 8(b). Indeed, the effective exchange current density decreases with the current decay, indicating a decrease of high exchange current density portion at the Ru–YSZ interface. Note that the fuel cell current does not decay as much as the fraction of anode exchange current density due to the compensating increase in the anode overvoltage. This is due to the overall decrease in relative cathode overvoltage and Ohmic losses following the current decay. As an overall result, oxidation state of Ru anode affects fuel cell current through change in the anode effective exchange current density and related overvoltage changes as expected from equation (4).

As seen in Fig. 8(a), the current shows a sudden recovery to its initial value. This is possibly due to reduction or removal of intermediates from the Ru surface which restores its catalytic activity. The oscillatory behavior can therefore be attributed to a repeated transition between two surface states of Ru; namely metal exposed state with high catalytic activity and an oxidized or intermediate covered state with low catalytic activity. The exact mechanism of the sudden surface cleaning is not well understood. One possibility is self-cleaning due to reaction between accumulated oxygen and methane reaction intermediates. Similar oscillation phenomenon was recently observed with Ni anodes with sulfur containing fuel under high fuel utilization condition [47]. The performance recovery in these oscillations was explained by the oxidation of adsorbed sulfur. Both Ru surface oxidation and adsorption of intermediates may lead to decrease in Ru catalytic activity. Analogous to the case of sulfur cleaning on Ni, performance recovery could be explained by Ru surface self-cleaning due to oxidation of adsorbed intermediate species. In order to further investigate and quantify the mechanism, in-operando studies such as utilizing synchrotron radiation X-ray absorption may be desirable.

4. Conclusions

μSOFCs utilizing sub-micrometer scale thin film multi-layers with Ru based anodes appear to be promising candidates for further studies to explore direct utilization of natural gas in the low temperature regime (400–550 °C). The μSOFCs with porous Ru anodes exhibited peak power density of 800 mW cm^{-2} at 530 °C with 3% humidified natural gas as the fuel. The performance of μSOFCs with dry methane and natural gas was comparable. Quasi-periodic oscillatory behavior of the cell current was observed when the μSOFC was continuously operated at constant voltage of 0.7 V. Through post-operation XPS analysis, it was found that the oxidation states of Ru anode surfaces after operation significantly differ depending on the fuel. The oxygen peak was stronger with methane and natural gas fueled anodes compared to as-prepared and hydrogen fueled anodes. A third oxide species at 532.2 eV appears after operation with hydrocarbon fuels and was attributed to oxygen related intermediate products of the methane electrochemical reaction. Mechanisms leading to the oscillatory behavior observed during extended operation are discussed based on Ru anode surface coverage states, effective exchange current densities and possible surface self-cleaning due to absorbed oxygen and reaction intermediates.

Acknowledgments

We are grateful to National Science Foundation Grant CCF-0926148 and SONY Corporation for financial support. KK was supported by the Department of Defense through the NDSEG fellowship. The authors thank Professor H. Yokokawa (AIST), Professor T. Ishihara (Kyushu University) and Q. Van Overmeere (Harvard) for valuable discussions.

References

[1] B.C.H. Steele, Nature 400 (1999) 619–621.
[2] D.J.L. Brett, A. Atkinson, N.P. Brandon, S.J. Skinner, Chemical Society Reviews 37 (2008) 1568–1578.
[3] R.J. Gorte, S. Park, J.M. Vohs, C.H. Wang, Advanced Materials 12 (2000) 1465–1469.
[4] S. McIntosh, J.M. Vohs, R.J. Gorte, Electrochemical and Solid-State Letters 6 (2003) A240–A243.
[5] L. Yang, S.Z. Wang, K. Blinn, M.F. Liu, Z. Liu, Z. Cheng, M.L. Liu, Science 326 (2009) 126–129.
[6] X.J. Chen, Q.L. Liu, S.H. Chan, N.P. Brandon, K.A. Khor, Electrochemistry Communications 9 (2007) 767–772.
[7] Y.B. Lin, Z.L. Zhan, J. Liu, S.A. Barnett, Solid State Ionics 176 (2005) 1827–1835.
[8] J.A. Liu, S.A. Barnett, Solid State Ionics 158 (2003) 11–16.
[9] K. Wang, R. Ran, Z.P. Shao, Journal of Power Sources 170 (2007) 251–258.
[10] T. Hibino, A. Hashimoto, M. Yano, M. Suzuki, M. Sano, Electrochimica Acta 48 (2003) 2531–2537.
[11] B.C.H. Steele, A. Heinzel, Nature 414 (2001) 345–352.
[12] K. Kerman, B.K. Lai, S. Ramanathan, Journal of Power Sources 196 (2011) 2608–2614.
[13] P.C. Su, C.C. Chao, J.H. Shim, R. Fasching, F.B. Prinz, Nano Letters 8 (2008) 2289–2292.
[14] A. Evans, A. Bieberle-Hutter, J.L.M. Rupp, L.J. Gauckler, Journal of Power Sources 194 (2009) 119–129.
[15] M.J. Hei, H.B. Chen, J. Yi, Y.J. Lin, Y.Z. Lin, G. Wei, D.W. Liao, Surface Science 417 (1998) 82–96.
[16] D. Qin, J. Lapszewicz, Catalysis Today 21 (1994) 551–560.
[17] S. Bebelis, S. Neophytides, N. Kotsionopoulos, N. Triantafyllopoulos, M.T. Colomer, J. Jurado, Solid State Ionics 177 (2006) 2087–2091.

[18] C. Elmasides, D.I. Kondarides, S.G. Neophytides, X.E. Verykios, Journal of Catalysis 198 (2001) 195–207.
[19] M.G. Poirier, J. Trudel, D. Guay, Catalysis Letters 21 (1993) 99–111.
[20] A.V. Simakov, S.N. Pavlova, N.N. Sazanova, V.A. Sadykov, O.I. Snegurenko, V.A. Rogov, V.N. Paramon, I.A. Zolotarskii, V.A. Kuzmin, E.M. Moroz, Chemistry for Sustainable Development 11 (2003) 263–270.
[21] M. Lo Faro, D. La Rosa, G. Monforte, V. Antonucci, A.S. Arico, P. Antonucci, Journal of Applied Electrochemistry 37 (2007) 203–208.
[22] Y. Takagi, S. Adam, S. Ramanathan, Journal of Power Sources 217 (2012) 543–553.
[23] Y. Takagi, B.K. Lai, K. Kerman, S. Ramanathan, Energy & Environmental Science 4 (2011) 3473–3478.
[24] J.T.S. Irvine, A. Sauvet, Fuel Cells 1 (2001) 205–210.
[25] J.X. Chen, C.C. Yao, Y.Q. Zhao, P.H. Jia, International Journal of Hydrogen Energy 35 (2010) 1630–1642.
[26] M.J. Saeki, H. Uchida, M. Watanabe, Catalysis Letters 26 (1994) 149–157.
[27] O.A. Marina, M. Mogensen, Applied Catalysis A – General 189 (1999) 117–126.
[28] S.D. Park, J.M. Vohs, R.J. Gorte, Nature 404 (2000) 265–267.
[29] J.R. Rostrupnielsen, J.H.B. Hansen, Journal of Catalysis 144 (1993) 38–49.
[30] A. Evans, M. Prestat, R. Tölke, M.V.F. Schlupp, L.J. Gauckler, Y. Safa, T. Hocker, J. Courbat, D. Briand, N.F. de Rooij, D. Courty, Fuel Cells 12 (2012) 614–623.
[31] K. Kerman, T. Tallinen, S. Ramanathan, L. Mahadevan, Journal of Power Sources 222 (2013) 359–366.
[32] M. Mogensen, K. Kammer, Annual Review of Materials Research 33 (2003) 321–331.
[33] B.K. Lai, K. Kerman, S. Ramanathan, Journal of Power Sources 196 (2011) 6299–6304.
[34] B. Kimmerle, A. Baiker, J.D. Grunwaldt, Physical Chemistry Chemical Physics 12 (2010) 2288–2291.
[35] Y.J. Kim, Y. Gao, S.A. Chambers, Applied Surface Science 120 (1997) 250–260.
[36] L. Atanasoska, W.E. Ogrady, R.T. Atanasoski, F.H. Pollak, Surface Science 202 (1988) 142–166.
[37] R. Schafranek, J. Schaffner, A. Klein, Journal of the European Ceramic Society 30 (2010) 187–192.
[38] D. Rochefort, P. Dabo, D. Guay, P.M.A. Sherwood, Electrochimica Acta 48 (2003) 4245–4252.
[39] S. Doniach, M. Sunjic, Journal of Physics Part C: Solid State Physics 3 (1970) 285–291.
[40] P. Van der Heide, X-ray Photoelectron Spectroscopy – an Introduction to Principles and Practices, John Wiley & Sons, Inc., New Jersey, 2012.
[41] A. Foelske, O. Barbieri, M. Hahn, R. Kotz, Electrochemical and Solid-State Letters 9 (2006) A268–A272.
[42] C. Mun, J. Ehrhardt, J. Lambert, C. Madic, Applied Surface Science 253 (2007) 7613–7621.
[43] W.E. O'Grady, L. Atanasoska, F.H. Pollak, H.L. Park, Journal of Electroanalytical Chemistry 178 (1984) 61–68.
[44] S.P. Sharma, L.L. Hines, IEEE Transactions on Components Hybrids and Manufacturing Technology 6 (1983) 89–92.
[45] J.Y. Shen, A. Adnot, S. Kaliaguine, Applied Surface Science 51 (1991) 47–60.
[46] Z. Cheng, J.H. Wang, Y.M. Choi, L. Yang, M.C. Lin, M.L. Liu, Energy & Environmental Science 4 (2011) 4380–4409.
[47] T. Yoshizumi, S. Taniguchi, Y. Shiratori, K. Sasaki, Journal of Electrochemical Society 159 (2012) F693–F701.